

Track Finding at Belle II

1

2 Belle II Tracking Group, Valerio Bertacchi^a, Tadeas Bilka^b, Nils Braun^c,
3 Giulia Casarosa^d, Luigi Corona^d, Sam Cunliffe^e, Filippo Dattola^e,
4 Gaetano De Marino^f, Michael De Nuccio^e, Giacomo De Pietro^g,
5 Giulio Dujany^h, Patrick Ecker^c, Michael Eliachevitchⁱ, Tristan Fillinger^h,
6 Oliver Frost^e, Rudolf Frühwirth^j, Uwe Gebauer^k, Sasha Glazov^e,
7 Nicolas Gosling^l, Aiqiang Guo^{e,m}, Thomas Hauth^c, Martin Heck^c,
8 Mateusz Kaletaⁿ, Jakub Kandra^b, Claus Kleinwort^e, Thomas Kuhr^l,
9 Simon Kurz^e, Peter Kvasnicka^b, Jakob Lettenbichler^j, Thomas Lueck^l,
10 Alberto Martini^g, Felix Metzner^c, Dmitrii Neverov^o, Carsten Niebuhr^e,
11 Eugenio Paoloni^d, Sourav Patra^p, Leo Piilonen^q, Cyrille Praz^e,
12 Markus Tobias Prim^c, Christian Pulvermacher^c, Sebastian Racs^c,
13 Navid Rad^e, Petar Rados^e, Martin Ritter^l, Giuliana Rizzo^d,
14 Armine Rostomyan^e, Bianca Scavino^r, Tobias Schlüter^s,
15 Benjamin Schwenker^k, Stefano Spataro^t, Björn Spruck^r, Henrikas Svidras^e,
16 Francesco Tenchini^e, Dong Thanh^u, Yuma Uematsu^v, James Webb^w,
17 Christian Wesselⁱ, Laura Zani^d

18 ^a *Scuola Normale Superiore and INFN Sezione di Pisa, Largo B. Pontecorvo 3, Pisa,*
19 *56127, Italy*

20 ^b *Charles Univ. Prague, Institute of Particle and Nuclear Physics, Ke Karlovu 3, Praha,*
21 *12116, Czechia*

22 ^c *Karlsruhe Institute of Technology (KIT), Institute of Experimental Particle Physics*
23 *(ETP), Wolfgang-Gaede-Str. 1, Karlsruhe, D-76131, Germany*

24 ^d *Dipartimento di Fisica, Università di Pisa and INFN Sezione di Pisa, Largo B.*
25 *Pontecorvo 3, Pisa, 56127 Italy*

26 ^e *Deutsches Elektronen-Synchrotron (DESY), Notkestrasse 85, Hamburg, D-22607,*
27 *Germany*

28 ^f *Laboratoire de L'accelerateur Lineaire (LAL) Orsay, Batiment 200 BP34 91898*
29 *ORSAY Cedex, France*

30 ^g *Dipartimento di Matematica e Fisica, Università di Roma Tre, I-00146 Roma INFN*
31 *Sezione di Roma Tre, Roma, I-00146, Italy*

32 ^h *Université de Strasbourg, CNRS, IPHC, UMR 7178, Strasbourg, 67037, France*

33 ⁱ *Rheinische Friedrich-Wilhelms-Univ. Bonn, Physikalisches Institut, Nussallee 12,*
34 *Bonn, D-53115, Germany*

35 ^j *Institut of High Energy Physics of the Austrian Academy of Sciences, Nikolsdorfer*
36 *Gasse 18, Wien, 1050, Austria*

37 ^k *University of Göttingen, Faculty of Physics, Friedrich-Hund-Platz 1, Göttingen,*
38 *D-37077, Germany*

39 ^l *Ludwig Maximilians Univ. München (LMU), Faculty of Physics,*

40 *Geschwister-Scholl-Platz 1, Munich, D-80539, Germany*
41 ^m *Institute of High Energy Physics (IHEP), 19B Yuquan Road, Beijing, 100049, China*
42 ⁿ *Institute of Nuclear Physics PAN, Division of Particle Physics and Astrophysics,*
43 *Department of Leptonic Interactions, ul. Radzikowskiego 152, Krakow, 31342, Poland*
44 ^o *Nagoya Univeristy, Graduate School of Science, Furou-cho Chikusa-ku, Aichi,*
45 *Nagoya-shi, 464-8602, Japan*
46 ^p *Indian Institute of Science Education and Research (IISER) Mohali, Knowledge city,*
47 *Sector 81, SAS Nagar, Manauli, Punjab, 140306, India*
48 ^q *Virginia Polytechnic Institute and State Univ., 315 A Robeson Hall, Blacksburg, VA*
49 *24061-0435, USA*
50 ^r *Johannes Gutenberg Univ. of Mainz, Johann-Joachim-Becher-Weg 45, Mainz,*
51 *D-55128, Germany*
52 ^s *LP-Research, Inc., Nishiazabu 1, Minato City, Tokyo, 106-0031, Japan*
53 ^t *INFN and Univ. Torino, Via P. Giuria 1 I, Torino, 10125, Italy*
54 ^u *Fudan University, Key Laboratory of Nuclear Physics and Ion-beam Application*
55 *(MOE) and Institute of Modern Physics, Shanghai, 200443, China*
56 ^v *Department of Physics, Graduate School of Science, The University of Tokyo, 7-3-1*
57 *Hongo, Bunkyo-ku, Tokyo 113-0033, Japan*
58 ^w *University of Melbourne, School of Physics, Melbourne, Victoria 3010, Australia*

59 **Abstract**

This paper describes the track-finding algorithm that is used for event reconstruction in the Belle II experiment operating at the SuperKEKB B-factory in Tsukuba, Japan. The algorithm is designed to balance the requirements of a high efficiency to find charged particles with a good track parameter resolution, a low rate of spurious tracks, and a reasonable demand on CPU resources. The software is implemented in a flexible, modular manner and employs a diverse selection of global and local track-finding algorithms to achieve an optimal performance.

60 **1. Introduction**

61 The SuperKEKB accelerator complex [1] located at Tsukuba, Japan is
62 designed to achieve a world-record instantaneous luminosity for e^+e^- collisions
63 of $8 \times 10^{35} \text{ cm}^{-2} \text{ s}^{-1}$. The collisions of 4 GeV positron and 7 GeV electron
64 beams are recorded by the upgraded successor of the Belle detector [2],
65 which is called Belle II [3]. The expected data sample with an integrated

66 luminosity of 50 ab^{-1} will allow the Belle II experiment to study B meson
67 decays with unprecedented accuracy.

68 The high instantaneous luminosity poses, however, several additional
69 challenges. The signal and background rates are expected to increase sig-
70 nificantly compared to those observed at Belle. The larger data samples
71 will act to reduce statistical uncertainties, this emphasizes the need to keep
72 systematic effects under control. The experiment therefore requires highly
73 performing track-finding software, capable to cope with high rates and sig-
74 nificant background, while maintaining high efficiency and resolution for par-
75 ticles with momenta as low as $50 \text{ MeV}/c$.

76 The track-finding algorithms used in Belle II are built on the experi-
77 ment's modular software framework [4] and can be combined for an optimal
78 overall performance. The algorithms use both local and global track-finding
79 methods based on cellular automaton [5, 6, 7, 8] and Legendre transfor-
80 mation [9], respectively, as well as combinatorial Kalman filter (CKF) ap-
81 proaches [10, 11, 12, 13]. A specific feature of the Belle II tracking is a
82 heavy use of multivariate methods, based on the gradient boosted decision
83 tree implementation provided by the FastBDT package [14], to improve back-
84 ground filtering and track-candidate search. The performance of the track
85 finding is estimated using a detailed simulation of the Belle II detector using
86 $\Upsilon(4S) \rightarrow B\bar{B}$ events with expected background overlaid.

87 The paper is organized as follows. Section 2 describes the main com-
88 ponents of the Belle II tracking devices: the silicon-based vertex detector
89 (VXD) and the central drift chamber (CDC). Properties of signal events and
90 background are discussed in Section 3. Section 4 describes the event simula-
91 tion and methods used to gauge the tracking performance. The description
92 of the reconstruction of hits in each of the tracking detectors is given next
93 in Section 5. The general strategy for track reconstruction is outlined in
94 Section 6 after which the CDC track finding is explained in Section 7. Track
95 finding with the silicon vertex detector (SVD) using the concept of dedicated
96 Sector Maps and a local track finding algorithm is discussed in Section 8
97 followed by the description of the CKF in Section 9. Section 10 presents
98 performance studies of the Belle II track finding using simulated events and
99 Section 11 summarizes the results.

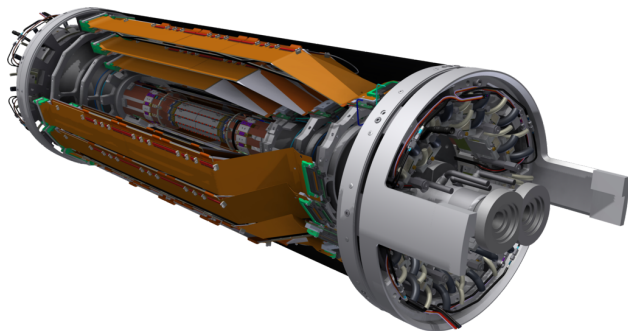


Figure 1: The Belle II Vertex Detector volume. The four outer layers are the silicon vertex detector and the pixel detector is in the center.

100 2. Belle II Tracking System

101 The trajectories of the charged long-lived decay products of the B mesons
 102 are measured by the Belle II tracking detectors: the silicon based vertex de-
 103 tector and the central drift chamber. The origin of most of these trajectories
 104 is in the proximity of the interaction point (IP). The trajectories pass through
 105 the beam pipe which is comprised of two thin walls of beryllium enclosing a
 106 duct through which liquid paraffin flows. The inner wall of the beam pipe
 107 is sputtered with a thin layer of gold to shield the VXD from synchrotron
 108 radiation. The beam pipe radiation length for particles crossing it at a 90°
 109 angle is 0.79%. A thin superconducting solenoid provides a magnetic field of
 110 about 1.5 T directed along the nominal mechanical axis of the CDC support
 111 cylinder. A system of final focusing quadrupole and compensating solenoid
 112 magnets is situated close to the IP. The field remains fairly homogeneous and
 113 varies on the order of 1% in the entire tracking volume.

114 In spherical coordinates, with the z axis parallel to the CDC axis of
 115 symmetry and directed along the boost direction, the CDC covers the θ range
 116 comprised between 17° and 150° and the full ϕ range. Just outside the CDC
 117 there are additional detectors for the reconstruction of neutral particles and
 118 particle identification.

119 A rendering of the VXD is shown in Figure 1. The VXD is composed of
 120 two detectors, the pixel detector (PXD) and the SVD, which are based on
 121 DEPFET [15] and double-sided silicon strip technologies, respectively. An
 122 overview of the key figures of the PXD is shown in Table 1. The PXD consists
 123 of two approximately cylindrical layers with radii of 14 and 22 mm. The inner
 124 (outer) layer contains eight (twelve) ladders with a size of approximately 1.5

Table 1: Specifications of the Belle II PXD.

Layer	Radius (mm)	Ladders	Sensors	Pixels/Sensor $u \times v$	Pitch $u \times v$ ($\mu\text{m} \times \mu\text{m}$)
1	14	8	16	250×768	50 × (55 to 60)
2	22	12	24	250×768	50 × (70 to 85)
Sum		20	40	7 680 000	

125 by 10 cm (1.5 by 13 cm). Each ladder is built by gluing two DEPFET modules
 126 together at their short edge. In total there are 40 PXD sensors. The ladders
 127 overlap with each other in r - ϕ (local u coordinate), while there is a 0.85 mm
 128 gap between the two sensors on each ladder in z (local v coordinate). The
 129 sensitive region of the PXD is 75 μm in thickness while the edges, which
 130 provide the mechanical stiffness to the structure and make the PXD ladder
 131 self-supporting, are 450 μm thick. One of the two long sides of each ladder
 132 is equipped with twelve switchers, six for each module. These switchers are
 133 the only PXD ASICs (Application Specific Integrated Circuits) inside the
 134 tracking volume. The other ASICs of the PXD are on the two short edges of
 135 each ladder in close contact to the cooling blocks that support the detector.
 136 The structure is extremely light with the equivalent thickness for a PXD
 137 layer of 0.2% of the radiation length. In both layers, the PXD pixel matrix
 138 is organized in rows comprising of 250 pixels with a pitch of 50 μm that run
 139 in the u direction, and columns comprising of 768 pixels with pitches varying
 140 between 55 μm and 85 μm that run along the v direction. In total the PXD
 141 comprises approximately eight million pixels.

Table 2: Specifications of the Belle II SVD.

Layer	Radius (mm)	Ladders	Sensors	Strips/Sensor u, v	Pitch u, v ($\mu\text{m}, \mu\text{m}$)
3	39	7	14	768, 768	50, 160
4	80	10	30	768, 512	75 to 50, 240
5	104	12	48	768, 512	75 to 50, 240
6	135	16	80	768, 512	75 to 50, 240
Sum		35	172	132 096, 91 648	

142 Table 2 shows the key figures of the SVD. The SVD consists of four
 143 layers of double-sided silicon strip detectors. All the layers have a barrel-

144 shaped part with rectangular sensors. The forward section of the outermost
 145 three layers has a lamp-shade geometry made of trapezoidal sensors. This
 146 setup minimizes the amount of material for the particles originating from
 147 the IP. The radii of the four SVD layers range from 39 mm to 135 mm. The
 148 layers consist of 7 to 16 ladders, with 2 to 5 sensors per ladder, respectively.
 149 Similarly to the PXD, the SVD ladders overlap in u while there is a 2 mm
 150 gap between the sensors on each ladder in v . Each sensor of the first layer
 151 of the SVD has 768 strips per side, with readout pitches of $50\ \mu\text{m}$ on the
 152 side measuring the u coordinate and $160\ \mu\text{m}$ on the side measuring the v
 153 coordinate. The barrel sensors of the three outer layers have 768 strips
 154 with a readout pitch of $75\ \mu\text{m}$ in u and 512 strips with a readout pitch of
 155 $240\ \mu\text{m}$ in v . The slanted sensors of these layers have the same number of
 156 strips in the respective directions, and the same pitch in v . The pitch in
 157 u -direction varies from $75\ \mu\text{m}$ at the back to $50\ \mu\text{m}$ at the front side, due to
 158 the trapezoidal shape. The readout strips are interleaved with floating strips
 159 to improve the spatial resolution. In total, there are 172 SVD sensors with
 160 about 220 thousand read-out strips. Each SVD sensor has a thickness of
 161 $320\ \mu\text{m}$. The contribution to the overall radiation length due to mechanical
 162 support structure, electronic read-out and cooling is kept at a minimum so
 163 that the material of the outer SVD layers is equivalent to 0.6% radiation
 164 length at normal incidence.

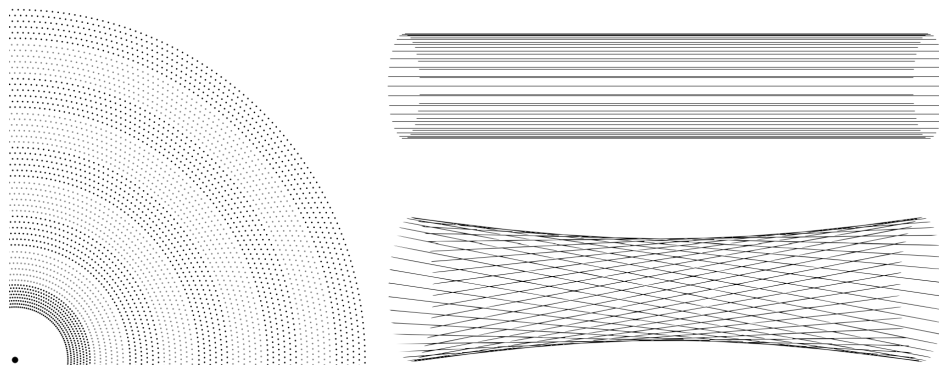


Figure 2: Left: A quadrant of a slice of the r - ϕ projection of the drift chamber. The innermost superlayer contains eight layers, all others contain six. Right: A visualization of stereo wires (bottom) relative to axial wires (top). The skew is exaggerated.

165 The main specifications of CDC are given in Table 3. The inner volume
 166 of the CDC contains about 50 000 sense and field wires, defining drift cells

Table 3: Specification of the Belle II CDC.

Layer	Radius of Sense Wires (mm)	Number of Wires	Drift Cell Size (cm)	Average Resolution (μm)
1 to 56	168 to 1111.4	160 to 384	~ 1 to ~ 2	120

167 with a size of about 2 cm. The electric field in the drift cells is approximately
 168 cylindrical leading to a two-fold ambiguity with the same drift time mea-
 169 sured for the tracks passing at the same distance on either side of the sense
 170 wire (*left-right passage* ambiguity). The sense wires are arranged in layers,
 171 where six or eight adjacent layers are combined in a superlayer, as seen in
 172 Figure 2. The outer eight superlayers consist of six layers with 160 to 384
 173 wires. The innermost superlayer has eight layers with 160 wires in smaller
 174 (half-size) drift cells to cope with the increasing background towards smaller
 175 radii. The superlayers alternate between axial (A) orientation, aligned with
 176 the solenoidal magnetic field, and stereo (U, V) orientation. Stereo wires
 177 are skewed by an angle between 45.4 and 74 mrad in the positive and neg-
 178 ative direction. The direction changes sign between U and V layers, with
 179 a total superlayer configuration of AUAVAUAVA. The drift distance resolu-
 180 tion of the drift chamber is about 120 μm . By combining the information of
 181 axial and stereo wires it is possible to reconstruct a full three-dimensional
 182 trajectory.

183 3. Belle II Events and Background

184 The events recorded by the Belle II experiment can be classified according
 185 to the e^+e^- scattering process occurring at the interaction point. The main
 186 category is composed of the $\Upsilon(4S)$ events in which the annihilation of an
 187 electron-positron pair produces an $\Upsilon(4S)$ resonance. This resonance decays
 188 promptly into a quantum entangled state of two B mesons. The B meson
 189 decay vertices have an average spatial separation of $\sim 130 \mu\text{m}$. Thus a track-
 190 ing detector resolution significantly better than that is required to resolve
 191 them. This is crucial for the measurements of the time dependent CP and T
 192 violation as well as tests of the CPT symmetry in the B meson system. The
 193 decay-vertex resolution relies on the spatial resolution of the PXD sensors as
 194 well as their proximity to the IP in order to reduce the extrapolation lever
 195 arm, and thus the effects of multiple Coulomb scattering on the measurement

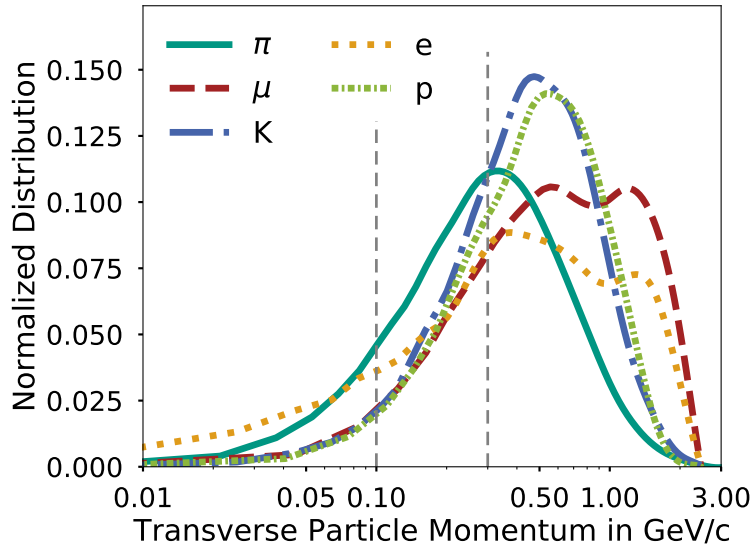


Figure 3: Transverse momentum distributions of primary charged particles as simulated for $\Upsilon(4S)$ events. A logarithmic scale is used for the x axis. The distribution of each charged particle type is normalized to the total number of tracks from the respective type. The vertical line at 100 MeV/c indicates the transverse momentum threshold below which a track can only be found by the SVD. Charged particles with transverse momenta below the value 300 MeV/c marked by the second vertical line can curl inside the CDC volume.

196 of the impact parameters.

197 Studies of (semi)leptonic B decays often require the reconstruction of
 198 the missing neutrino by exploiting four-momentum conservation. Hence the
 199 tracking algorithm needs to find all of the charged final state particles. This
 200 is demanding since there are about 11 tracks per event on average. Moreover,
 201 the momentum spectrum of the particles is quite soft, ranging from a few
 202 tens of MeV/c to a few GeV/c (Figure 3). It is also essential to keep the rate
 203 of fake and duplicate tracks as low as possible.

204 The reconstruction of particles with momenta below 200 MeV/c is par-
 205 ticularly challenging since the trajectories are heavily affected by multiple
 206 Coulomb scattering and by energy loss in the material. Moreover, only the
 207 measurements of the four layers of the SVD are available to the pattern
 208 recognition algorithms for most of the tracks in this low momentum region.
 209 The soft momentum spectrum is also challenging for the CDC since particles
 210 with momenta below 300 MeV/c can loop several times in the CDC volume

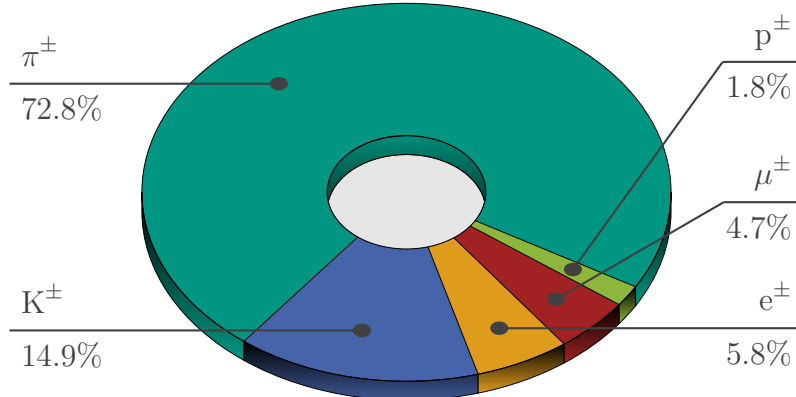


Figure 4: Fractions of charged particle types in generic $\Upsilon(4S)$ events.

211 producing hundreds of hits. The relative abundance of the long lived charged
 212 particles produced in $\Upsilon(4S)$ decays is illustrated in Figure 4.

213 Other categories of events are also of importance to the experiment. Most
 214 notably τ -pair and $c\bar{c}$ events improve the existing limits and measurements
 215 on the τ lepton sector and on the charmed mesons. The experiment will also
 216 be used to search for non-Standard Model particles, i.e. dark photons, axion-
 217 like particles, or magnetic monopoles that might be produced directly in
 218 e^+e^- collisions. These events are characterized by a lower track multiplicity,
 219 a stiffer momentum spectrum, and by a less spherical event topology.

220 Particles lost by beam-gas and Touschek scattering, as well as due to
 221 non-linearities of the machine lattice, lead to additional hits in the detec-
 222 tor. The occupancy due to this machine background is expected to be very
 223 high as a consequence of the high beam currents, small emittances, and large
 224 beam-beam tune shifts needed to reach the design luminosity [16]. The elec-
 225 tromagnetic processes occurring at the interaction point, radiative Bhabha
 226 and electron-positron pair production, whose cross sections are of the order
 227 of several mb, are going to be the leading effects for the beam particle loss
 228 rate at nominal luminosity.

229 The VXD occupancy is expected to be largely dominated by soft electron-
 230 positron pairs produced at the IP by the process $e^+e^- \rightarrow e^+e^-e^+e^-$. The
 231 forward and backward sections of the SVD may be hit by an electromagnetic
 232 shower originating from Bhabha electrons interacting in the support structure
 233 of the final focusing magnets. The number of background hits exceeds the

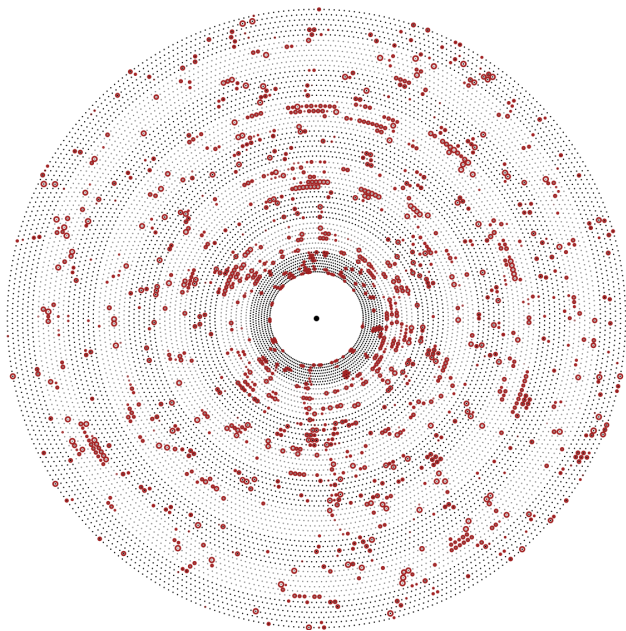


Figure 5: CDC measurements produced by simulated beam-induced background anticipated for the nominal instantaneous luminosity.

234 signal hits by two orders of magnitude resulting in a PXD inner layer pixel
 235 occupancy close to 2% and an SVD inner layer strip occupancy close to 3%.

236 The CDC occupancy is also expected to be dominated by the hits left by
 237 particles coming from electromagnetic showers initiated by beam particles.
 238 These interact with the material around the final focusing magnets which are
 239 well inside the CDC volume. Figure 5 shows the CDC measurements pro-
 240 duced by simulated beam-induced background for the nominal instantaneous
 241 luminosity.

242 4. Simulation and Track Finding Efficiency Definition

243 A full simulation tool based on Geant4 [17] is used to model the detector
 244 and collider properties. Using the information from the particle generator
 245 and the Geant4 simulation of the particles traversing the detector volume,
 246 an ideal track finder, called Monte Carlo (MC) track finder, is implemented.
 247 Its performance is limited only by the detector acceptance, efficiency and
 248 resolution, and by definition cannot be surpassed. A set of figures of merit
 249 has been developed to qualify and tune the track finding algorithms. The

250 analysis is limited to tracks identified by the MC track finder (MC-tracks from
251 now on) having enough hits to completely determine the five parameters of
252 the helix-like trajectory. A good track finding algorithm should behave as
253 closely as possible to the MC track finder. In particular, each track should
254 be assigned all of the hits of one and only one MC particle. Two figures of
255 merit are defined for each pair of MC-track and a track found by the pattern
256 recognition (PR-track):

- 257 • The *hit efficiency* quantifies how efficient the pattern recognition is in
258 identifying *all* the hits belonging to a single particle. It is defined as
259 the fraction of hits of a given MC-track contained in a given PR-track.
260 Ideally, there should be one and only one PR-track containing all the
261 hits of a given MC-track, thus the *hit efficiency* should be 100% for the
262 correct pair and zero for all others.
- 263 • The *hit purity* quantifies how precise the pattern recognition is in iden-
264 tifying the hits belonging to *only one* particle. It is defined as the
265 fraction of hits of a given PR-track contained in a given MC-track.
266 Ideally, there should be one and only one MC-track to which all the
267 hits of a given PR-track belong, thus the *hit purity* should be 100% for
268 the correct pair and zero for all others.

269 A PR-track is defined as *matched* to a given MC-track if the hit purity
270 exceeds 66% and the hit efficiency exceeds 5%. The low hit efficiency re-
271 quirement accounts for low momentum tracks curling in the tracking volume
272 which may leave several hundred of hits.

273 If there are two or more PR-tracks that are matched to the same MC-
274 track, the PR-track with the highest hit purity is defined as the correctly
275 identified match and the remaining PR-tracks are defined as *clones*. If mul-
276 tiple PR-tracks have the same hit purity, the hit efficiency is used in addition
277 to the purity to identify the match. The *track finding efficiency* is defined as
278 the fraction of matched MC-tracks over all MC-tracks.

279 If the PR-track fails the purity requirement, e.g. the PR-track is made
280 up of hits from two MC-tracks, each one with a hit purity below 66% or the
281 PR-track is made of background hits, it is defined as a *fake*.

Table 4: Cluster position resolutions for different cluster sizes (one, two and larger than two) and strip pitch, evaluated on MC simulation. Resolutions are measured as 68% coverage of the residual distributions.

Sensor	Side	Pitch (μm)	Resolution (μm)		
			Size = 1	Size = 2	Size > 2
Layer 3	u	50	5.2	3.7	7.6
	v	160	18.1	12.1	18.0
Slanted	u	52–75	6.8	4.5	8.6
	v	240	34.4	18.0	21.4
Barrel	u	75	7.7	5.1	8.8
	v	240	24.8	17.1	20.5

282 5. Input to Tracking Algorithms

283 *PXD Reconstruction*

284 In order to reduce the Belle II data rate to an acceptable level, events are
 285 required to pass a software-based high-level trigger (HLT). Data from the
 286 PXD do not contribute to the HLT decision, and are therefore buffered in
 287 the readout chain. In case an event is accepted, the track information from
 288 the HLT is used to define so-called *Regions Of Interest* (ROIs) on the PXD
 289 planes. Only PXD hits within these ROIs are stored.

290 Neighboring pixels with a charge above a threshold are combined into
 291 clusters. The cluster position and charge are taken as input for the tracking
 292 algorithm.

293 *SVD Reconstruction*

294 The SVD reconstruction software provides in addition to cluster charge
 295 and position information also cluster time information to the tracking algo-
 296 rithms.

297 SVD clusters are formed by combining adjacent strips with a signal-over-
 298 noise ratio (SNR) above three. At least one strip in the cluster is required
 299 to have a SNR above five. The charge of the cluster is computed as the sum
 300 of the charges of the strips, while the cluster time and position are evaluated
 301 as the charge-weighted average of the strip times and positions, respectively.
 302 The cluster position resolution depends on the cluster size and strip pitch,
 303 as shown in Table 4.

304 The creation of space points follows the clustering and is achieved by
 305 combining all clusters on one side of a sensor with clusters on the other

306 side. The only requirement is that the cluster time (on both sides) is greater
307 than a minimum value. The cluster time information helps to reject the
308 majority of the out-of-time clusters, created by beam-background particles
309 produced before, or after the collision event of interest. The SVD cluster time
310 resolution varies between 2 ns (for Bhabha events) and 4 ns (hadronic events),
311 being slightly better on the v side due to a faster response of the electronics
312 on that side. The good time resolution allows the algorithm to reject 60% of
313 the background space points, while retaining 100% of the interesting ones.
314 The cluster time information provided by the SVD is also used later in the
315 reconstruction, in the pattern recognition step, as described in Section 8.

316 *CDC Reconstruction*

317 The front-end read-out electronics of the CDC use a time-to-digital con-
318 verter with a 1 ns resolution. This is used to measure the time between the
319 event's trigger signal and the arrival of the drift electrons at the sense wire,
320 the so-called *drift time*. With the $x-t$ relation function, which is an approx-
321 imation between drift time and distance parameterized in various areas of
322 the CDC, the actual relative distance between the sense wire and a passing
323 particle can be computed and used for track finding purposes. An additional
324 front-end read-out provides amplitude information, sampled at 33 MHz. This
325 information is used for the determination of the energy loss, employed by the
326 particle identification. It can also be used to separate signal and background
327 hits.

328 **6. High-Level Description of the Tracking Setup**

329 The Belle II software uses data processing *modules*, written in C++,
330 which are loosely coupled and transfer data via a common exchange con-
331 tainer. This allows for the reconstruction task to be split into different sub-
332 tasks which can be placed into a chain of independent and interchangeable
333 modules performing the corresponding task. The `RecoTrack` class is used as
334 a common exchange format between algorithms to transfer track candidates
335 from the different tracking detectors and their respective hits or clusters. The
336 final output of the track reconstruction is the `Track` class, which provides
337 the fitted track parameters for the analysis user.

338 The track trajectories are represented locally using the helix parameter-
339 ization, see Figure 6. The three helix parameters in the $x-y$ plane are: the
340 signed distance of the point of closest approach (POCA) to the z axis, d_0 ;

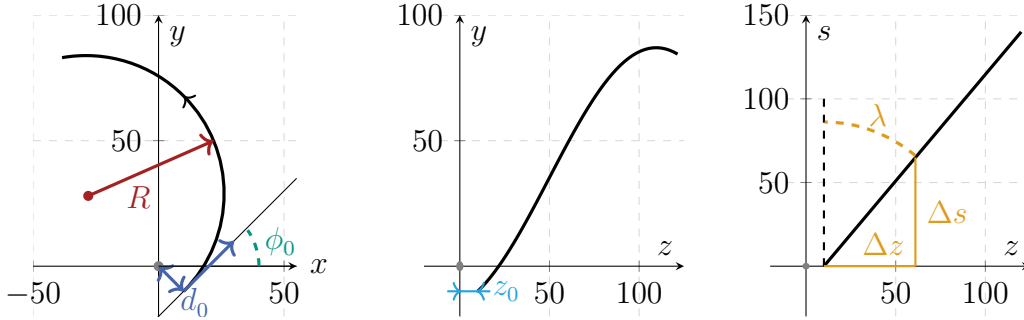


Figure 6: A schematic representation of the track’s trajectory in the x - y (left), z - y (middle) and z - s (right) projections. All dimensions are in cm. The track parameters are: d_0 , the signed distance of the closest approach to the z axis (POCA); ϕ_0 , the angle defined by the x axis and the track transverse momentum at the POCA; z_0 , the z coordinate at the POCA; and λ , the track dip angle. Also shown is the track radius R , which is the inverse of the absolute value of the track curvature ω .

341 the angle defined by the x axis and the track transverse momentum at the
 342 POCA , ϕ_0 ; and the track curvature signed with the particle charge, ω . The
 343 helix can be represented by a straight line in the s - z space, with s being
 344 the path length along the circular trajectory in the x - y projection. The two
 345 corresponding parameters are: the z coordinate at d_0 , z_0 ; and the tangent of
 346 the dip angle $\tan \lambda$.

347 Figure 7 shows an overview of the steps performed for track reconstruction
 348 at Belle II. Due to the very different properties of the three tracking
 349 detectors, different algorithms are used for each of them. As a first step, the
 350 measured signals in the CDC are filtered and reconstructed by two independ-
 351 ent algorithms: a global track finding based on the Legendre [9] algorithm
 352 and a local algorithm employing a cellular automaton. The results of both
 353 algorithms are merged and the CDC-only tracks are fitted employing a deter-
 354 ministic annealing filter (DAF) [18]. A combinatorial Kalman filter (CKF)
 355 is used to enrich the CDC tracks with SVD clusters. High-curvature tracks that
 356 did not produce enough hits in the CDC are reconstructed with a standalone
 357 SVD track finder using an advanced filter concept called Sector Map and a
 358 cellular automaton. The results are combined, fitted again with a DAF and
 359 extrapolated to the PXD with a second CKF. At this step the track finding
 360 stage is complete. The following sections describe these steps in more detail.

361 The final step after the track finding includes a track fit using the DAF
 362 provided by the GENFIT2 [18] package. For the fit, a specific particle hy-

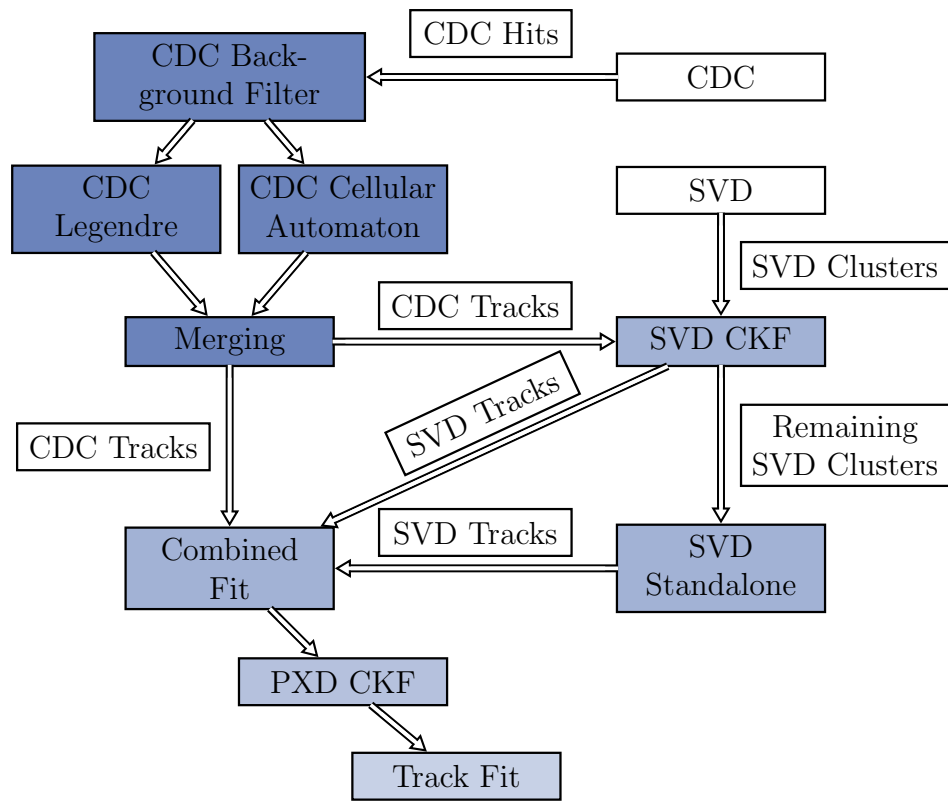


Figure 7: Overview of the steps performed for track reconstruction at Belle II. See text for more details.

363 pothesis must be assumed to calculate the energy loss and the material effects
364 correctly. In Belle II, all reconstructed tracks are fitted with the π , K and p
365 hypotheses. The results of the fit is stored to be used in physics analyses.

366 7. CDC Algorithm

367 Two distinct algorithms are used for the track finding in the CDC: global,
368 and local track finding. This enables a high track-finding efficiency while
369 keeping the fake rate low. The global track finding searches for patterns of
370 hits consistent with helix trajectories, even with missing hits, while the local
371 track finding detects extended patterns of nearby hits.

372 Both algorithms make use of the specific geometry of the CDC and ex-
373 ploit the flexibility of the software framework. The software is written in a
374 modular manner allowing for different sequences of algorithms. Currently,
375 the global track finding is performed first, after the initial filtering of the
376 CDC hits. Thus the global algorithm serves as the primary finding algo-
377 rithm, which is followed by the local track finding algorithm. The latter
378 helps with reconstructing displaced tracks which originate far away from the
379 interaction point. The track candidates of both algorithms are then merged
380 and post-processing is performed to remove falsely attached hits and, poten-
381 tially, to attach additional ones. The reconstructed tracks are then passed
382 to the DAF algorithm to be fitted.

383 *Global CDC Track Finding*

384 The global track finding in the CDC is based on the Legendre transfor-
385 mation [9]. It is first performed in the r - ϕ plane, using wire information from
386 axial layers only. After that, it is extended to the three-dimensional space, by
387 attaching wires from stereo layers to existing r - ϕ trajectories. The primary
388 target of the algorithm is finding tracks originating from the vicinity of the
389 origin in r - ϕ . It is adjusted to identify also slightly offset tracks.

390 In the first step of the algorithm, the position information in axial layers
391 is approximated by drift circles. These drift circles are calculated using
392 a calibrated x - t relation and time information corrected for particle time-
393 of-flight and signal propagation time along the sense wire. For the time
394 propagation correction, it is assumed that particle trajectories are straight
395 lines from the origin, that particles travel with the speed of light, and that
396 they cross the sense wires in the middle. These assumptions are revised when
397 the track parameters are determined.

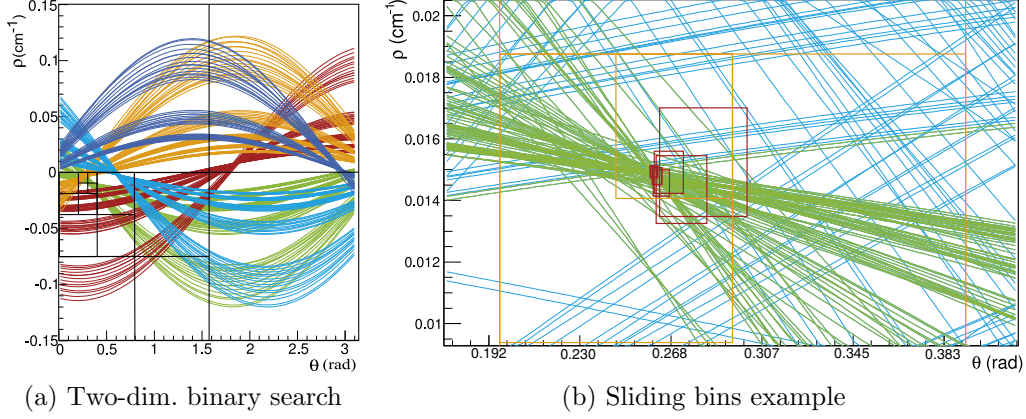


Figure 8: Examples of: (a) standard two-dimensional binary search algorithm; (b) modified algorithm with variable bin size. See text for more details.

398 The reconstruction in the r - ϕ plane continues with a conformal mapping
 399 with the center at the origin. This operation transforms circular trajectories
 400 starting from the origin to straight lines while the drift circles remain circles.
 401 The track finding in the conformal space is thus reduced to the determination
 402 of straight lines tangential to a set of circles.

The equation of a tangent to a drift circle in conformal space can be represented using the two Legendre parameters ρ and θ as

$$\rho = x_0 \cos \theta + y_0 \sin \theta \pm R_{\text{dr}} ,$$

403 where (x_0, y_0) and R_{dr} represent the center of the circle and its radius, re-
 404 spectively. Hence, each drift circle maps to a pair of sinusoids in the ρ - θ
 405 track-parameter space. The track recognition and track parameter determi-
 406 nation correspond to finding the most populated regions in the ρ - θ space. An
 407 efficient method to localize these regions is a two-dimensional binary search
 408 algorithm, as illustrated in Figure 8a. The algorithm consists of dividing the
 409 ρ - θ space into four equally sized bins and selecting the most populated of
 410 them for further subdivision, until convergence.

411 The two-dimensional binary search algorithm uses a dedicated *quad tree*
 412 data structure to store intermediate search results. Each node in the quad
 413 tree is linked to four children, corresponding to four sub-bins of the node. In
 414 general, the search is continued only for the sub-bin containing the most hits.
 415 However, it is possible to step back and examine other directions, without

416 repeating the search from the beginning, which speeds up the search for
417 multiple track candidates.

418 The binary search stops when the bin size becomes smaller than a reso-
419 lution parameter that is taken to be dependent on ρ . This accounts for the
420 smearing of the track parameters due to the energy loss, non-uniformity of
421 the magnetic field, displaced IP, uncertainty of the drift circle radii and wire
422 displacements. The resolution function is optimized using simulated events.

423 The introduction of the resolution function as the stopping criterion al-
424 lows to extend the algorithm to non-standard bin sizes. For a track that is
425 displaced from the origin, the crossing points in the Legendre space may be
426 split between two bins. This effect can be reduced greatly by allowing for
427 overlapping bins. Bins extended by 25% with respect to the exact division
428 are used. A positive side effect of this feature is that the overlapping bins
429 tend to *slide* towards the maximal density of intersections, as illustrated in
430 Figure 8b.

431 Multiple tracks are found iteratively, using several passes over the Leg-
432 endre space. At each pass a new track candidate is declared to be found
433 when it satisfies certain quality criteria, such as the number of attached hits.
434 These quality criteria can be varied to increase finding efficiency for different
435 track topologies. Hits corresponding to the found track candidates are re-
436 moved from further iterations. The high-momentum tracks crossing all CDC
437 layers are searched for first, followed by curling tracks and tracks with large
438 longitudinal momentum, which leave the chamber at smaller radii.

439 The r - ϕ track candidates are subjected to a post-processing step, per-
440 formed in the physical r - ϕ space using the fast fitting algorithm of [19].
441 Firstly, the track candidates are checked to see if they can be merged, to
442 reduce the clone rate. The merge algorithm uses a χ^2 -based criterion, com-
443 paring the quality of the circular fits to the hits from the separate track-
444 candidates to the fit to the combined set of hits. In addition, hits from the
445 track candidates are examined to determine if they have to be removed or re-
446 assigned to other tracks. Finally, all unassigned hits are checked to determine
447 if they can be attached to the existing track candidates.

448 Hits from stereo layers, containing z information, are added to the r - ϕ
449 trajectories at the next step. The r - ϕ trajectory is used to reconstruct the
450 position information of each stereo measurement. As the stereo wire can be
451 approximated by a straight line and the drift circle does not have direction
452 information, finding the position gives two solutions: either the drift circle is
453 enclosed by the trajectory circle, or not — giving two possible position values

454 for each hit. Stereo hits with a reconstructed z coordinate z_{rec} determined far
 455 outside the detector volume are dismissed. Given that z_{rec} depends strongly
 456 on the estimated r -position of the trajectory at the stereo wire which may
 457 be not very accurate, hits as far as twice the physical drift chamber length
 458 are retained.

The problem of track finding becomes very similar to the search in the conformal mapping of the r - ϕ space which makes it possible to use the same algorithm as described above. This time, the trajectory is straight in the s - z space and it can be described by the equation

$$z_0 = z_{\text{rec}} - \tan \lambda \cdot s_{\text{rec}} ,$$

459 with s_{rec} being the path to the stereo-wire hit. This gives a line of possible
 460 trajectory parameters $(z_0, \tan \lambda)$ for each stereo-layer hit. The point with the
 461 most intersections of the lines in the parameter space is used to determine
 462 the track parameters. For this, an analogous implementation of the quad
 463 tree algorithm as described above is used.

464 The stereo-wire hits that are found are added to the r - ϕ track only in the
 465 case they are not selected for another r - ϕ track. In the latter case the hits
 466 are not added to any track which increases the purity of the hit assignment.

467 *Local CDC Track Finding*

To complement the global search approach, and to detect short tracks and tracks displaced from the IP with a high efficiency, the local track finder operates without any assumption on the origin of tracks. The algorithm searches for connected hits in the CDC superlayers, so called segments. This search uses the cellular automaton concept, which acts on an acyclic graph of vertices connected by edges. More specifically, a weighted cellular method is used, where the vertex i has the weight Θ_i and the edge between the vertices i and j has the weight w_{ij} . Now, track finding can be formulated as maximization of an energy function which can be formulated with

$$E_i = \sum w_{ij} + \sum \Theta_j ,$$

468 where the sums are taken along a path to the vertex i . The concept of the
 469 weighted cellular automaton is employed in two different stages:

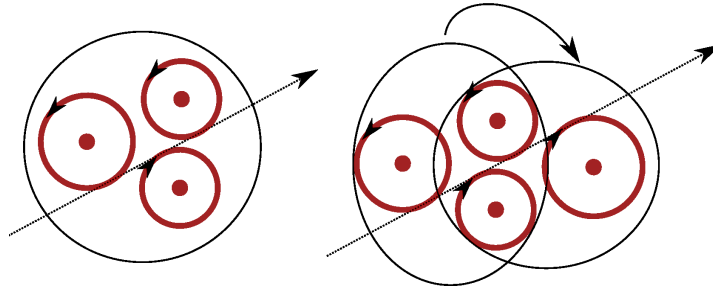


Figure 9: Combination of three neighboring wire hits to a graph vertex (left) and two triplets sharing two wire hits to a graph edge (right).

470 *Segment building stage.* Vertices (*triplets*) are formed by combining three
 471 neighboring hits and assuming the left-right passage hypotheses for a unique
 472 trajectory through these three hits¹. A linear trajectory is then extracted
 473 from the measured drift circles by a least-squares method and the weight
 474 Θ_j is assigned based on the χ^2 value of the fit. Edges are created from
 475 neighboring triplets that share two hits and which pass loose feasibility cuts,
 476 with the weight w_{ij} determined based on the χ^2 value of the straight line fit
 477 to the four drift circles (see Figure 9). The algorithm allows for information
 478 missing from one CDC layer.

479 *Track building stage.* This stage combines the individual segments found in
 480 the axial and stereo superlayers to longer tracks. The vertices are created
 481 from a pair of segments in neighboring axial- and stereo-wire superlayers.
 482 The weight Θ_j of each vertex is computed with a χ^2 circle fit using the Rie-
 483 mann method [20] and the reconstruction of the z coordinate is performed
 484 using a linear fit in the s - z space. Neighboring vertices that share one seg-
 485 ment form the edges in the cellular automaton's graph (see Figure 10). The
 486 corresponding weight w_{ij} is computed based on the χ^2 value of the fit to
 487 hits from all segments. Additional information, such as the number of hits
 488 per segment, can be included in the weight calculation using multivariate
 489 analysis methods.

¹In general, several triples are built for a given set of three neighboring hits, depending on the left-right passage hypothesis.

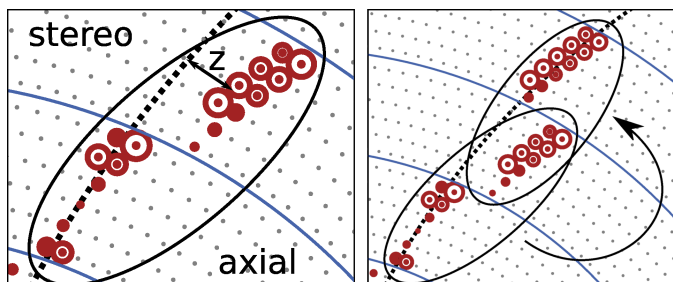


Figure 10: Combination of a pair of axial- and stereo-wire segments to one graph vertex (left) and the combination of vertices, that share one segment, to a graph edge (right).

490 *Combination of Local and Global Tracking Results*

491 The two track finding algorithms described above are both used to find
 492 tracks from the full set of CDC hits. This is done to exploit their specific
 493 benefits, with the global track finding capable to reconstruct tracks with
 494 several missing layers and the local track finding having similar efficiency
 495 regardless of the track origin.

496 For combining the results of both tracking approaches, the track candi-
 497 dates from the global track finder are used as a baseline. Segments found
 498 by the local track finder are added to those tracks using a multivariate ap-
 499 proach. The track-segment combination is based on FastBDT [14], which
 500 uses several variables calculated from the track and the segment (e.g. the
 501 number of common hits, helix parameters, hit-to-trajectory distances) into
 502 one single number, which classifies between correct and wrong matches. The
 503 multivariate method is trained using simulated events.

504 Several quality filters based on multivariate estimators are applied to the
 505 found tracks and their hits. This increases the hit purity, improves the track
 506 parameter resolution, and decreases the rate of fake and clone tracks.

507 **8. SVD Standalone Algorithm**

508 A dedicated standalone algorithm is employed for the task of track find-
 509 ing with the SVD. This algorithm reconstructs the low momentum particles
 510 with a transverse momentum of less than 100 MeV/c which deposit too few
 511 hits in the CDC. However, due to the proximity of the SVD to the beam,
 512 the algorithm has to cope with a high occupancy from beam-induced back-
 513 ground. The original idea and implementation for this algorithm, called the
 514 VXD Track Finder (VXDTF), is described in [21]. Further improvements of

515 the algorithm, which are partly described in [22] and [23], led to its second
516 version, VXDTF2.

517 The input to the VXDTF2 algorithm is the set of the three dimensional
518 space points created in the pre-processing steps described in Section 5 from
519 the SVD measurements². The VXDTF2 algorithm consists of three steps.
520 In the first step, graphs of related space points are created using geometrical
521 information. A map, called a Sector Map [24], containing the geometrical
522 relations between different regions of the silicon detector as well as additional
523 selection criteria, supplies the necessary input for this step. The prepared
524 graphs are then evaluated in the second step by a cellular automaton which
525 yields a set of paths. As third step, the final set of SVD track candidates is
526 chosen by selecting the best paths.

527 *Sector Map*

528 The Sector Map is a data structure that holds information about how
529 space points in different regions of the detector can be related by tracks.
530 To cope with the high number of possible combinations of space points, the
531 sectors on sensor concept — originally proposed in [24] — is used for track
532 finding with the SVD. This concept consists in subdividing each sensor into
533 smaller sections, called *sectors*. The default setup is a division of each sensor
534 element into three parts along its width and three parts along its length,
535 resulting in nine sectors per sensor. It is possible to adjust the number
536 of sectors individually for each sensor, which allows the granularity to be
537 adapted to changing detector conditions during the run time of Belle II.
538 This representation of the SVD geometry allows to define directed relations
539 between sectors of the detector which commonly contain measurements of
540 the same track, as illustrated in Figure 11, where the sectors 6 and 15 are
541 related due to the track traversing both sectors. The direction of the relations
542 is defined by the order in which the sectors are traversed. A mapping among

² It is also possible to use the three dimensional measurements provided by the PXD. However, due to the combined effect of its proximity to the beam line and the lower readout frequency of its sensors, the PXD is subject to a substantially higher occupancy from beam-background induced hits. Omitting the PXD measurements from the track-finding process simplifies the combinatorial problem and leads to a purer set of track candidates produced by the standalone algorithm. The task of evaluating the additional information available in the measurements of the PXD is passed on to a dedicated algorithm described in Section 9.

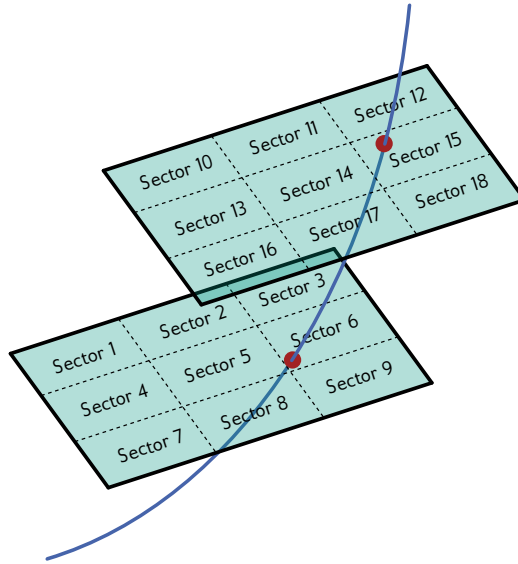


Figure 11: Illustration of the subdivision of two sensors into nine sectors each and of the relation between the sectors 6 and 15 which are traversed by the same track.

543 sectors defined by these relations allows for a significantly reduced number
 544 of combinations of space points as input to the algorithm.

545 In addition to the relations between sectors of the detector geometry, the
 546 Sector Map holds selection criteria to be fulfilled by combinations of space
 547 points on related sectors. These criteria are called *filters* and are defined
 548 for pairs of two as well as triplets of three space points. They provide a
 549 way to reject background hits and thereby a further reduction of the space
 550 point combinations to be evaluated per event. Each filter is a function which
 551 calculates a specific quantity, called *filter variable*, for a given space point
 552 pair or triplet, and checks if the result is within a given validity range. The
 553 validity range depends on the filter variable and on the sectors. It is stored for
 554 each individual sector combination alongside the respective relation between
 555 sectors in the Sector Map. Filter variables are mostly geometrical quantities
 556 derived from the spatial information of the space points, or are calculated
 557 from the precise timing information provided by the SVD.

558 The variables calculated for filters for space point pairs are simple quanti-
 559 ties such as distances between the two space points (in one-, two-, and three-
 560 dimensions), angles in ϕ - and θ -direction defined by the two space points,
 561 or the difference in their detection times. An illustration of the combined

562 application of a selection of such filters is depicted in Figure 12.

563 More complicated quantities can be evaluated for filters based on the
564 combination of three space points. These include for example the angle en-
565 closed by the two segments defined by the three space points, or the position
566 of the center as well as the radius of the circle defined by the three space
567 points in the x - y plane. Space point triplet filters based on the SVD timing
568 information are also employed. As the SVD is composed of only four layers
569 and a triplet of space points already provides enough degrees of freedom to
570 unambiguously define a helix trajectory of a charged particle in a magnetic
571 field, further filters for combinations of four and more space points are not
572 considered.

573 The directed relations between sectors as well as the filter selection criteria
574 are obtained via a training process based on Monte Carlo events. For this
575 purpose, a dedicated sample of representative $\Upsilon(4S)$ events is generated.
576 Track candidates are selected from this training sample using the MC track
577 finder (see Section 4). Additional samples of high-momentum tracks such
578 as simulated high-momentum muon events or simulated Bhabha events can
579 be incorporated into the training process as $\Upsilon(4S)$ events don't typically
580 produce such tracks. Based on this set of tracks, directed relations between
581 pairs of sectors are obtained for all pairs of sectors which have been traversed
582 subsequently by at least one track. The selection ranges for the filters are
583 defined by the minima and the maxima or by quantiles of the distributions
584 of the respective filter variables as observed during the training for each
585 individual sector combination.

586 This training process allows the Sector Map to learn the geometry of the
587 SVD setup. Hence, it can adapt to changing detector conditions like defects
588 on the sensors or even the loss of complete sensors or layers, as long as these
589 defects are modeled by the simulation. The Sector Maps produced in this
590 manner are stored in the database of Belle II, which allows defining different
591 Sector Maps for different run conditions.

592 *Track Finding Algorithm*

593 To address the high combinatorics during the process of building track
594 candidates from the space points provided by the SVD, the Sector Map filters
595 are used. A first directed graph, called *sector network*, is build for an event
596 with all active sectors (sectors on which hits are detected) as nodes. The
597 edges connecting the nodes of the sector network are given by the directed
598 relations stored for the respective active sectors in the Sector Map.

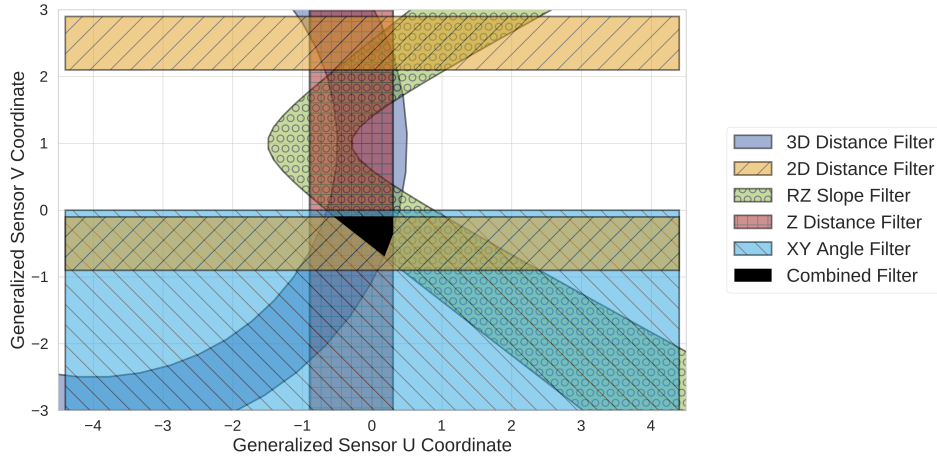


Figure 12: Illustration of the selection power of the combination of several Sector Map filters. The illustration depicts a sensor plane and the areas selected by several Sector Map filters calculated for a given space point on another sensor layer. Only space points within these areas are allowed to be combined with the given space point on the other layer. The combination of all filters reduces the allowed region to the area shown in black.

599 The next step comprises the creation of a second directed graph with the
600 space points on the active sectors of an event as nodes. The edges of this
601 *space point network* are given by the edges of the sector network and connect
602 space points in pairs if they pass the criteria of the Sector Map filters for
603 space point pairs. Their directions are defined by the respective edges in the
604 sector network. The resulting space point pairs are called *segments*. Next,
605 pairs of such segments that have a space point in common are combined
606 into triplets of space points, creating a third directed graph with segments
607 as nodes, which is therefore referred to as a *segment network*. Again, the
608 criteria given by the respective filters for space point triplets provided by
609 the Sector Map are considered during the combination of the segments to
610 triplets.

611 All paths given by the edges of the segment network with a minimal
612 length of three space points are considered as track candidates without fur-
613 ther restrictions from the Sector Map. A cellular automaton is used to gather
614 the longest paths in the graph, beginning with the nodes on the outermost
615 layers as these are least occupied by beam-background induced hits.

616 Gathered this way, the track candidates in an event may share SVD clus-
617 ters or even space points. At this stage of the algorithm, the number of fake

618 and clone track candidates make up more than half of the track candidates
619 and are directly related to the overlaps among a set of tracks. To reduce
620 the fraction of fakes and clones, the final set of track candidates for an event
621 is required to be composed only of candidates which do not share any SVD
622 clusters among them. As roughly 5% of all tracks in a normal $\Upsilon(4S)$ event
623 share at least one SVD cluster with another track, this introduces a small
624 loss of less than 1% in finding efficiency to the benefit of an increase in purity
625 for the final set of track candidates by a factor of roughly two. Any cases
626 where two or more track candidates share common hits are resolved based
627 on a rating of all track candidates, followed by a greedy local selection as
628 explained in the following paragraphs.

629 For the rating of each track candidate, a quality indicator determined
630 from the goodness of a fast fit to the candidate is employed. The fit method
631 used for this objective is an adapted version of the Triplet Fit introduced
632 in [25]. This method is chosen because it takes into account the multiple
633 scattering relevant for the tracks left by low momentum particles of interest
634 to the VXD standalone track finding. The Triplet Fit is applied to each path
635 supplied by the cellular automaton, as well as their subpaths obtained by
636 excluding one or multiple space points from the original path. The latter
637 allows for the exclusion of misattributed space points and results in a track
638 candidate with higher purity. Furthermore, the inclusion of the subpaths can
639 lead to a recovery of the efficiency loss due to overlapping true tracks. When
640 creating the subpaths, the rule of a minimal length of three space points is
641 still obeyed.

642 The Triplet Fit yields a χ^2 value for each track candidate by combining
643 fits to all space point triplets contained within a candidate under consid-
644 eration of the effect of multiple scattering. For this estimate the average
645 radiation length of the SVD sensor material as reported in [3], as well as a
646 first approximation of the entrance angle of the particle with respect to the
647 sensor plane are taken into account. The p -value is calculated for each track
648 candidate from its χ^2 value and degrees of freedom and used as a quality
649 indicator. Based on these quality indicators, the final set of non-overlapping
650 track candidates is chosen via a greedy selection which takes the candidate
651 with the highest quality indicator among the ones competing for a space
652 point.

653 Optionally, a multivariate method can be applied which combines the ac-
654 quired quality indicator with further features, such as a particle momentum
655 estimate, the number of space points and properties of the involved SVD

656 clusters. This approach can yield a quality indicator with an enhanced per-
657 formance. For this purpose a FastBDT is trained on Monte Carlo events
658 obtained by applying the candidate creation steps up to the point of the
659 Triplet Fit. In the resulting training sample, the track candidates with a
660 purity of 100% are marked as truth target. Therefore, a FastBDT trained
661 in this manner has learned to identify track candidates with a high purity.
662 Enabling this auxiliary multivariate analysis method for the overlap removal
663 increases the achieved track finding efficiency, albeit with a significant drop
664 in hit efficiency. This option is not therefore used as a basis for the resolu-
665 tion of overlaps, but used to produce a refined track quality estimate in an
666 additional step. This indicator of the track quality is stored for all tracks
667 of the final set and can later be accessed and used in the event selection of
668 physics analyses.

669 The algorithm is further optimized as it is found to perform more slowly
670 than acceptable at the HLT for certain peculiar Bhabha events. The slow-
671 down is understood as follows. In rare cases, highly energetic electrons scat-
672 ter in the material of the final focusing magnets, thereby causing a shower
673 of secondary particles which leave a large number of clusters in a small area
674 of the SVD. This leads to a significant increase in the combinatorics during
675 the candidate creation process that cannot be restricted by the Sector Map
676 filters. To tackle this issue, two additional measures are incorporated into
677 the candidate creation. Firstly, a limit on the number of nodes and edges
678 in the three networks is introduced, as the problematic Bhabha events can
679 mostly be identified based on noticeably high values for these quantities. If
680 the limits determined on Monte Carlo simulations are exceeded, the process-
681 ing of the event is aborted and the problematic event is marked as such. The
682 limits are chosen so that the desired measurements of the $\Upsilon(4S)$ resonance
683 are not affected. Secondly, during the path-collection step an additional se-
684 lection procedure based on the segment network is applied, which evaluates
685 overlaps already in this graph. All paths associated with a given segment are
686 grouped together and evaluated with the Triplet Fit. Only a fixed number
687 of best candidates from each group is considered for further processing steps.
688 This early candidate reduction based on space point pair overlaps imposes
689 an additional limit on the combinatorics for problematic events which slip
690 through the aforementioned limits. By means of these additional selection
691 steps, the problematic events can be handled by the VXDTF2 and the run
692 time limits imposed by the requirements of the HLT are satisfied.

693 9. Combinatorial Kalman Filter

694 The combinatorial Kalman filter (CKF) is widely used in tracking in
695 high-energy physics experiments [10, 11, 12, 13]. One of the advantages of
696 the method is that it produces tracks with high purity also in environments
697 of high hit densities. The CKF is an iterative local algorithm and was first
698 described in [26]. Starting with a seed estimation of the track parameters
699 with uncertainties, the track is extrapolated with the Runge-Kutta-Nyström
700 method [27] into the detector volume. Hereby, non-uniform magnetic fields
701 are included in the numerical solution of the equation of motion. A correction
702 of the energy and the uncertainties due to energy loss and multiple scattering
703 can optionally be included. After the extrapolation, possible hit candidates
704 are determined based on the current position and uncertainties of the track
705 candidate. The next hit candidate is added to the track and the procedure
706 is repeated. If there are multiple mutually exclusive next-hit candidates, the
707 whole track candidate is duplicated and subsequently treated as two tracks.
708 In the end, the final track candidate is selected according to different quality
709 criteria.

710 As a first step, the track candidates found by the CDC track finding algo-
711 rithm are used as seeds to attach SVD space points. Hereby, low momentum
712 tracks can have both start and end points in the inner layers of the CDC, so
713 both points can be used as a possible seed to account for wrongly assigned
714 charges in the CDC. The CDC seeds are fitted using a DAF algorithm as-
715 suming a pion mass hypothesis. These seeds are iteratively extrapolated to
716 the SVD sensors and SVD space points are attached. Material effects are dis-
717 regarded at this stage to increase the processing speed. Due to the complex
718 detector layout, the different use cases, and the complex input data from the
719 CDC track finding algorithm, the filter decisions in the CKF are taken by
720 a FastBDT trained on simulated events including the beam-induced back-
721 ground. Variables such as the distance between extrapolated and measured
722 hit position as well as the calculated χ^2 of the hit are taken into account.
723 They are enriched with information about the track candidate, for example
724 the number of attached space points or the estimated transverse momentum.
725 The number of track candidates that are processed in parallel is restricted
726 to ten to keep the computational effort on a manageable level. After a final
727 candidate selection based on FastBDT using full-track information such as
728 the summed χ^2 and the number of missing layers, the combined CDC-SVD
729 track is refitted using another DAF with a full material effect handling.

730 Due to hit inefficiencies of the CDC algorithm, especially for the stereo
731 layers, the track resolution can be extremely poor when $|z_0|$ is above 1 cm.
732 Therefore, it is not possible to attach SVD space points reliably to every
733 reconstructed CDC track. To solve this issue and to find additional low-
734 momentum tracks, the VXDTF2 described in Section 8 is applied to the
735 set of remaining space points in the SVD. The merging of additional SVD
736 candidates with unmerged CDC tracks is performed by a second pass of the
737 CKF. These unpaired CDC tracks are used as seeds and only space points
738 found by the VXDTF2 are allowed as input. Compared to the first pass of the
739 CKF with all space points, simpler filters are applied during the processing
740 due to the high purity of the VXDTF2 algorithm.

741 All reconstructed CDC-SVD tracks are then used to extract regions of
742 interest in the PXD during the online reconstruction. In the offline recon-
743 struction, the PXD clusters collected in these regions of interest are used
744 as input to the last application of the CKF and are attached to their com-
745 bined CDC-SVD tracks. The implementation is based on the same general
746 principles as the SVD CKF. It uses the same FastBDT filters which are now
747 applied to the PXD clusters. An additional input in the BDT classification
748 is given by the position and the shape of the PXD clusters.

749 The precise positions of the PXD clusters in the tracks improve the reso-
750 lution on the spatial track parameters d_0 and z_0 by a factor of two and more.
751 The efficiency of attaching SVD (PXD) hits is over 85% (89%). The purity
752 of the attached SVD or PXD hits is above 98% and 96%, respectively.

753 10. Performance of the Track Finding

754 The following section describes the performance of the tracking algorithms
755 presented in this paper. The performance is evaluated on an independent set
756 of simulated $\Upsilon(4S)$ events, including beam-induced background simulated
757 for the anticipated full instantaneous luminosity of $8 \times 10^{35} \text{ cm}^{-2} \text{ s}^{-1}$. In the
758 simulation, a detector setup with nominal positions is used. The results of the
759 reconstruction are compared to the respective MC tracks. Quantities such
760 as the purity or efficiency are calculated on this sample using the definitions
761 from Section 4. All quoted uncertainties on these quantities are calculated
762 using the method of bootstrapping [28].

763 Figure 13 shows the track-finding efficiency for different simulated trans-
764 verse momenta and different levels of beam-induced background relative to
765 the anticipated level. A distinction between final-state particles stemming

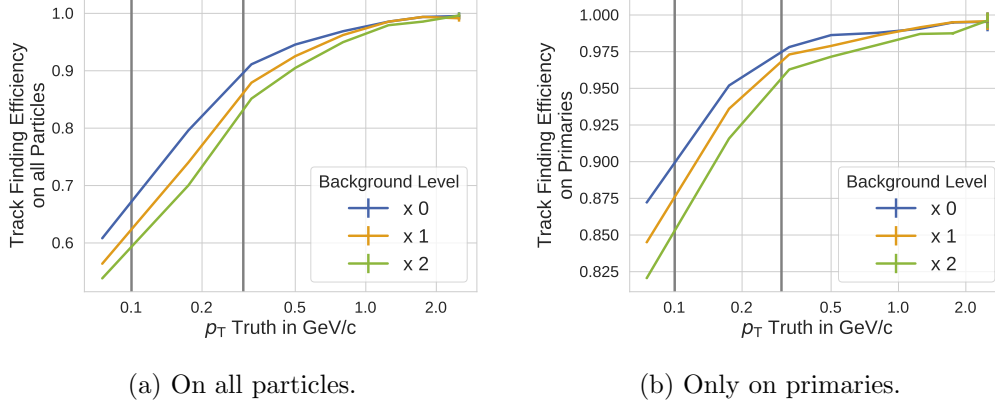
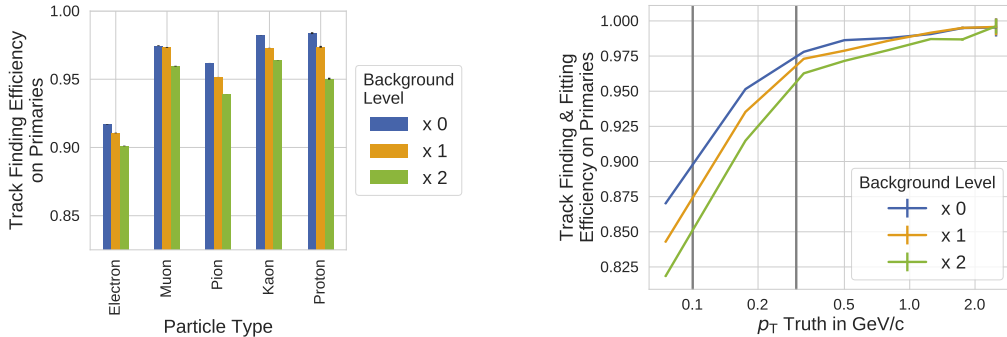


Figure 13: Track finding efficiency calculated for simulated $\Upsilon(4S)$ events with different levels of beam-induced background relative to the expected level. Figure 13a is calculated on all trackable simulated particles, whereas Figure 13b only takes into account trackable particles from the primary interaction. The gray vertical lines indicate the typical transverse momentum of particles only trackable in the VXD (below left line) and with high efficiency in the CDC (above right line).

766 from the primary e^+e^- interaction and decays of short-lived particles, pro-
 767 duced by event generators (*primaries*), and all final-state particles including
 768 those produced by Geant4 during the travel through the detector (*second-*
 769 *aries*) is made. Most of the analyses rely only on the former, whereas the
 770 latter can give valuable additional information for decays in flight or for
 771 particle identification. Comparing with the momentum spectrum shown in
 772 Figure 3, the efficiency for most of the charged particles expected at typi-
 773 cal Belle II collisions is higher than 93% for up to two times the expected
 774 beam background. Tracks with transverse momenta below 100 MeV/c im-
 775 pose complex problems to the track finding due to the small number of hits,
 776 high multiple scattering and the high level of background in the innermost
 777 layers. As a result, the efficiency decreases. The difference between the
 778 non-background and the expected beam background is small.

779 In Figure 14a the finding efficiency on primaries is compared for different
 780 simulated particle types. Due to the different interaction of electrons with the
 781 material, their trajectories are more likely to differ from the nominal helical
 782 path, making their reconstruction more challenging. However, the Belle II
 783 algorithms are able to achieve high efficiencies for every shown particle type
 784 for up to twice the expected beam background level.



(a) Track finding efficiency extracted for the most important particle types present in the primary $B\bar{B}$ -decays at Belle II dependent on the beam-induced background level. The overall finding efficiency is dominated by pions. (b) Calculated finding efficiency for those tracks, which are also successfully fitted by the DAF algorithm dependent on the beam-background level. The difference with respect to Figure 13b is negligible.

Figure 14: Finding efficiency by particle type and combined finding and fitting efficiency.

785 After the final fit with the DAF provided by GENFIT2 the tracks are
 786 extrapolated to the POCA to the origin to extract their helix parameters. In
 787 the following, only the results for the pion hypothesis are shown, as most of
 788 the produced charged final-state particles are pions.

789 As a first result, Figure 14b shows the finding efficiency calculated only
 790 with those tracks, where the GENFIT2 fit converged and the extrapolation
 791 succeeded. As expected, the difference to Figure 13b is negligible demonstrat-
 792 ing that the track finding algorithms deliver high-quality track candidates to
 793 the fitting algorithm.

The helix parameters of the tracks at the POCA can then be compared to the MC truth values. The resolution r_x is calculated as the 68% coverage of the the residual x between reconstructed and truth value given as

$$r_x = P_{68\%} (|x - P_{50\%}(x)|) ,$$

794 where P_q calculates the q -th percentile of a distribution. For a Gaussian
 795 distribution, the 68% coverage and the standard deviation agree. For non-
 796 Gaussian distributions the coverage is more robust against outliers. As only
 797 the results calculated with the pion hypothesis are shown, only true pions
 798 from $\Upsilon(4S)$ decays are taken into account for this study.

799 In Figure 15, the resolution as a function of the truth transverse momen-
800 tum is shown for the helix parameters d_0 and z_0 , and for p_T (the transverse
801 momentum). Both of the spatial parameters, d_0 and z_0 , are mainly influenced
802 by the precise PXD measurements. Due to the application of the CKF in the
803 PXD and the combination of the VXDTF2 and the CKF for the SVD, a high
804 precision (which is almost independent of the background level) is achieved.
805 The resolution of the extracted transverse momentum follows expectation:
806 as smaller momenta are more strongly influenced by multiple scattering and
807 a smaller number of measurable hits in the detector, the resolution decreases
808 with smaller transverse momenta.

809 Tracking is one of the most complex tasks in the reconstruction. It there-
810 fore requires a large fraction of the processing time allocated for the online
811 reconstruction on the HLT. In Figure 16 the processing time of different
812 components of the online reconstruction performed on one of the HLT worker
813 nodes is shown. Due to the higher number of tracks in $\Upsilon(4S)$ events, tracking
814 takes longer in this category. The track fitting, vertexing, and the track-based
815 collision time (T_0) extraction are heavily influenced by the handling of the
816 detector geometry in the software. Different techniques are planned to fur-
817 ther optimize the time spent in the geometry navigation. This is expected
818 to decrease the total processing time significantly which would allow to in-
819 troduce additional higher level algorithms for the HLT decision. However,
820 even with the large contribution to the total processing time from tracking,
821 a stable reconstruction on the HLT has been achieved.

822 11. Summary

823 The Belle II track-reconstruction software consists of multiple independ-
824 ent algorithms to process the measurements of each tracking detector and
825 integrate all available information into one final set of tracks available for
826 physics analyses. This allows the use of different algorithms whose properties
827 are especially suited for the three different tracking detectors. Ultimately, the
828 software provides a set of tracks based on the measurements of all tracking
829 detectors, thereby alleviating the complex task of track combination which
830 would otherwise be forced on physics analyses.

831 One challenge in this approach is to perform the combination of the tracks
832 reconstructed in each of the tracking detectors without increasing the fake
833 and clone rate. The best method to achieve this for the Belle II experiment

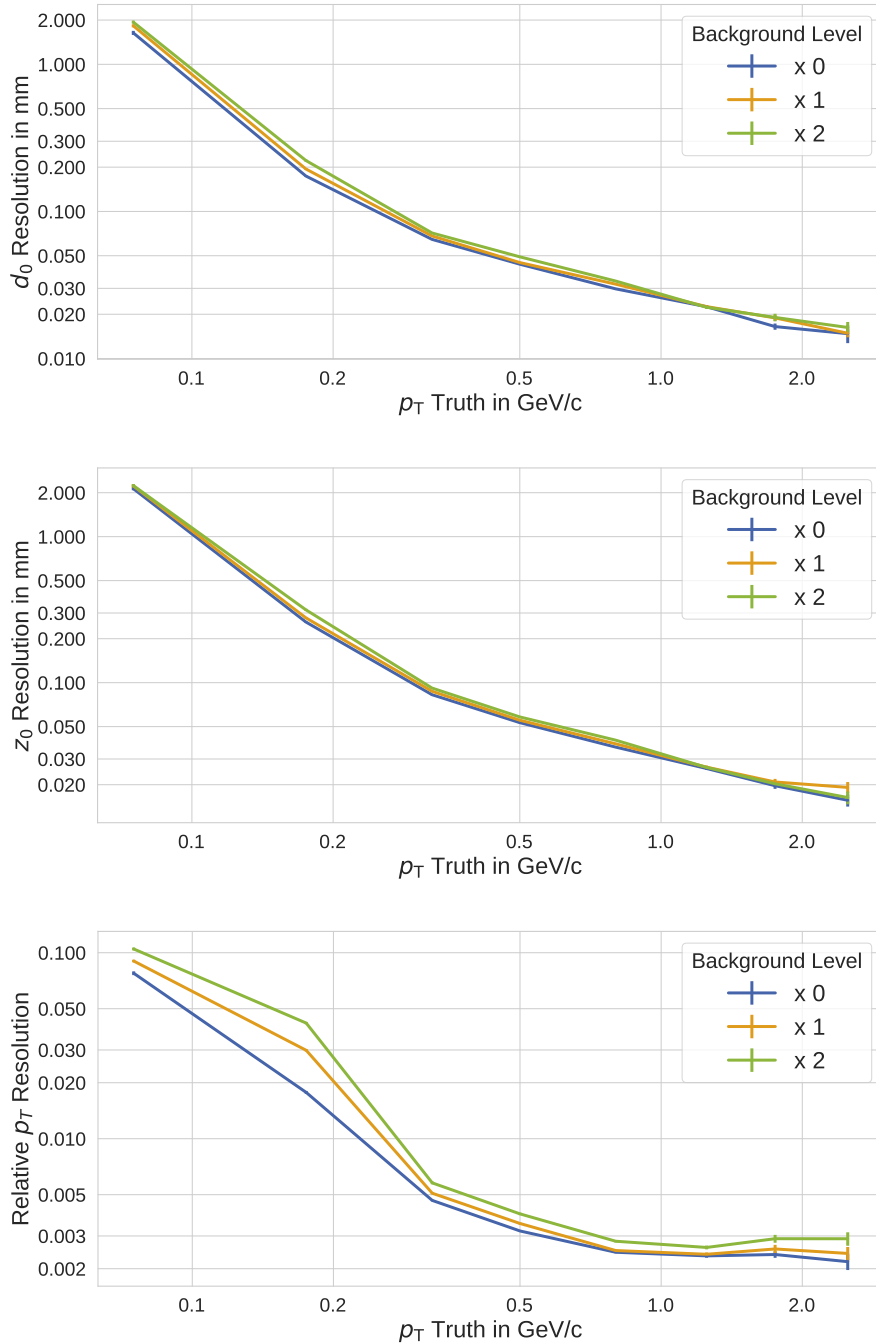


Figure 15: Resolutions for typical simulated $\Upsilon(4S)$ events with different levels of beam-induced background. As most of the simulated final state particles are pions, only the results of this fit hypothesis are shown.

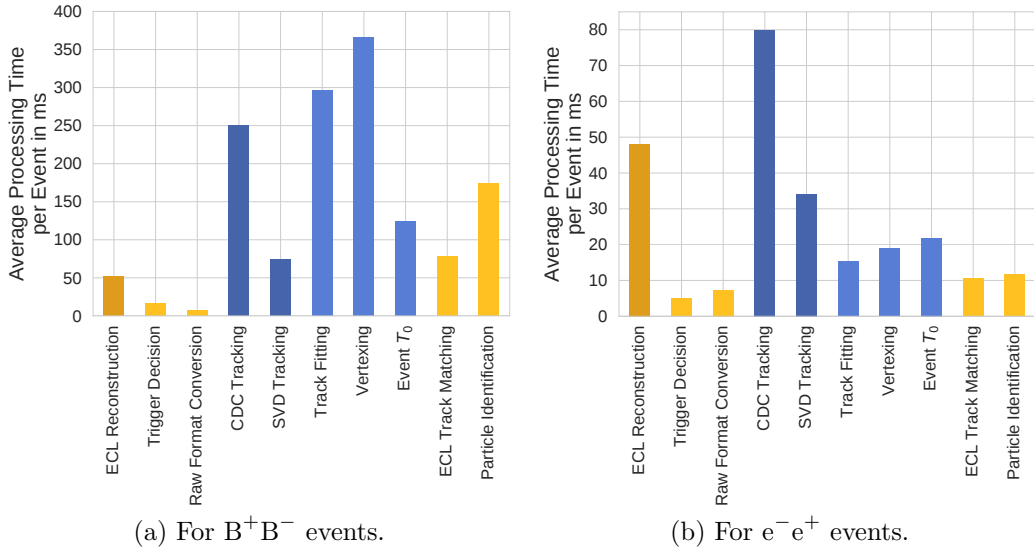


Figure 16: Processing time of a standard online reconstruction performed on the anticipated HLT worker nodes in single-processing mode for different event types. The components marked in dark (light) blue can be related to track finding (track fitting and other tracking-related tasks). The abbreviation *ECL* refers to the electromagnetic calorimeter of the Belle II experiment.

834 turned out to be a Combinatorial Kalman Filter to link hits and tracks across
835 detector boundaries.

836 The upgraded SuperKEKB collider will have much higher beam back-
837 ground radiation and the newly developed tracking algorithms are designed
838 to address this. Here, multiple methods like early background hit filter-
839 ing using multivariate methods and a fine-grained candidate selection using
840 the Sector Map concept are used. The studies with simulated background
841 environments at design luminosity of the accelerator show that tracking per-
842 formance remains adequate for the expected background rate.

843 The Belle II track-reconstruction software has been extensively studied
844 and used for the reconstruction of simulated events. In the years 2018 and
845 2019, the software was also employed during the first data taking of colli-
846 sion data and performed well for the commissioning of the Belle II detector,
847 studies of the background rates, and first physics results.

848 12. Acknowledgments

849 We would like to acknowledge the contributions of Karol Adamczyk,
850 Bozek Andrzej, Kirill Chilikin, David Dossett, Torben Ferber, Stefan Fer-
851 stl, Renu Garg, Hadrien Grasland, Yinghui Guan, Yoshihito Iwasaki, Pe-
852 ter Kodys, Ilya Komarov, Jo-Frederik Krohn, Miriam Künzel, Stefano La-
853 caprara, Klemens Lautenbach, Frank Meier, Moritz Nadler, Benjamin Ober-
854 hof, Hitoshi Ozaki, Johannes Rauch, Jonas Roetter, Michael Schnell, Alexei
855 Sibidanov, Marko Staric, Jacek Stypula, Maiko Takahashi, Umberto Tam-
856 poni, Viktor Trusov, Makoto Uchida, Jonas Wagner, Ian James Watson,
857 Jarek Wiechczynski and Michael Ziegler to the development of the Belle II
858 tracking software.

859 [1] Y. Ohnishi, T. Abe, T. Adachi, et al., Accelerator design at Su-
860 perKEKB, Progress of Theoretical and Experimental Physics 2013 (3)
861 (2013) 3A011–0. doi:10.1093/ptep/pts083.
862 URL [https://academic.oup.com/ptep/article-lookup/doi/10.](https://academic.oup.com/ptep/article-lookup/doi/10.1093/ptep/pts083)
863 [1093/ptep/pts083](https://academic.oup.com/ptep/article-lookup/doi/10.1093/ptep/pts083)

864 [2] J. Brodzicka, T. Browder, P. Chang, et al., Physics achievements
865 from the Belle experiment, Progress of Theoretical and Exper-
866 imental Physics 2012 (1) (2012) 4D001–0. arXiv:1212.5342,
867 doi:10.1093/ptep/pts072.

- 868 URL <https://academic.oup.com/ptep/article-lookup/doi/10.1093/ptep/pts072>
869
- 870 [3] T. Abe, I. Adachi, K. Adamczyk, et al., Belle II Technical Design Re-
871 portarXiv:1011.0352.
872 URL <http://arxiv.org/abs/1011.0352>
- 873 [4] T. Kuhr, C. Pulvermacher, M. Ritter, T. Hauth, N. Braun, The Belle
874 II Core Software, Computing and Software for Big Science 3 (1) (2019)
875 1. arXiv:1809.04299, doi:10.1007/s41781-018-0017-9.
876 URL <http://link.springer.com/10.1007/s41781-018-0017-9>
- 877 [5] M. Gardner, Mathematical Games – The fantastic combinations of John
878 Conway’s new solitaire game life, Scientific American 223(4) (1970) 120–
879 123. doi:10.1038/scientificamerican1070-120.
- 880 [6] A. Glazov, I. Kisel, E. Konotopskaya, G. Ososkov, Filtering tracks in dis-
881 crete detectors using a cellular automaton, Nucl. Instrum. Meth. A329
882 (1993) 262–268.
- 883 [7] I. Abt, I. Kisel, S. Masciocchi, D. Emelyanov, CATS: A cellular au-
884 tomaton for tracking in silicon for the HERA-B vertex detector, Nucl.
885 Instrum. Meth. A489 (2002) 389–405. doi:10.1016/S0168-9002(02)
886 00790-8.
- 887 [8] D. Funke, T. Hauth, V. Innocente, et al., Parallel track reconstruction
888 in CMS using the cellular automaton approach, J. Phys. Conf. Ser. 513
889 (2014) 052010. doi:10.1088/1742-6596/513/5/052010.
- 890 [9] T. Alexopoulos, M. Bachtis, E. Gazis, G. Tsipolitis, Implementation of
891 the Legendre Transform for track segment reconstruction in drift tube
892 chambers, Nuclear Instruments and Methods in Physics Research Sec-
893 tion A: Accelerators, Spectrometers, Detectors and Associated Equip-
894 ment 592 (3) (2008) 456–462. doi:10.1016/j.nima.2008.04.038.
895 URL <https://www.sciencedirect.com/science/article/pii/S0168900208005780>
896 [https://linkinghub.elsevier.com/retrieve/
897 pii/S0168900208005780](https://linkinghub.elsevier.com/retrieve/pii/S0168900208005780)
- 898 [10] R. Mankel, A. Spiridonov, The Concurrent Track Evolution algo-
899 rithm: extension for track finding in the inhomogeneous magnetic

- 900 field of the HERA-B spectrometer, Nuclear Instruments and Meth-
901 ods in Physics Research Section A: Accelerators, Spectrometers,
902 Detectors and Associated Equipment 426 (2-3) (1999) 268–282.
903 doi:10.1016/S0168-9002(99)00013-3.
904 URL [http://linkinghub.elsevier.com/retrieve/pii/
905 S0168900299000133](http://linkinghub.elsevier.com/retrieve/pii/S0168900299000133)
- 906 [11] R. Mankel, Pattern recognition and event reconstruction in particle
907 physics experiments, Reports on Progress in Physics 67 (4) (2004) 553–
908 622. arXiv:0402039, doi:10.1088/0034-4885/67/4/R03.
909 URL <http://arxiv.org/abs/physics/0402039>
- 910 [12] CMS Collaboration, Description and performance of track and primary-
911 vertex reconstruction with the CMS tracker, Journal of Instrumenta-
912 tion 9 (10) (2014) P10009–P10009. arXiv:1405.6569, doi:10.1088/
913 1748-0221/9/10/P10009.
914 URL <http://arxiv.org/abs/1405.6569>
- 915 [13] ATLAS Collaboration, Performance of the ATLAS Track Reconstruc-
916 tion Algorithms in Dense Environments in LHC Run 2, The Euro-
917 pean Physical Journal C 77 (10) (2017) 673. arXiv:1704.07983,
918 doi:10.1140/epjc/s10052-017-5225-7.
919 URL <http://arxiv.org/abs/1704.07983>
- 920 [14] T. Keck, FastBDT: A Speed-Optimized Multivariate Classification
921 Algorithm for the Belle II Experiment, Computing and Software
922 for Big Science 1 (1) (2017) 2. arXiv:1609.06119, doi:10.1007/
923 s41781-017-0002-8.
924 URL <http://arxiv.org/abs/1609.06119>
- 925 [15] J. Kemmer, G. Lutz, New Detector Concepts, Nuclear Instruments and
926 Methods in Physics Research 253 (1987) 365–377.
927 URL [https://ac.els-cdn.com/0168900287905183/
928 1-s2.0-0168900287905183-main.pdf?_tid=
929 9c6da4c9-b91f-464b-ae11-89016a3e2531&acdnat=1524476602_
930 881ecbe6d098bc1af5882f526389be5a](https://ac.els-cdn.com/0168900287905183/1-s2.0-0168900287905183-main.pdf?_tid=9c6da4c9-b91f-464b-ae11-89016a3e2531&acdnat=1524476602_881ecbe6d098bc1af5882f526389be5a)
- 931 [16] P. M. Lewis, et al., First Measurements of Beam Backgrounds at Su-
932 perKEKB, Nucl. Instrum. Meth. A914 (2019) 69–144. arXiv:1802.
933 01366, doi:10.1016/j.nima.2018.05.071.

- 934 [17] S. Agostinelli, J. Allison, K. Amako, et al., Geant4a simulation toolkit,
935 Nuclear Instruments and Methods in Physics Research Section A:
936 Accelerators, Spectrometers, Detectors and Associated Equipment
937 506 (3) (2003) 250–303. doi:10.1016/S0168-9002(03)01368-8.
938 URL [https://www.sciencedirect.com/science/article/
939 pii/S0168900203013688](https://www.sciencedirect.com/science/article/pii/S0168900203013688)[https://ac.els-cdn.com/
940 S0168900203013688/1-s2.0-S0168900203013688-main.pdf?_tid=
941 2ab2887a-7a2b-4813-9966-25cc44845930&acdnat=1524482129_
942 7273334d05ad6f2c66d093ae3c67b132](https://ac.els-cdn.com/S0168900203013688/1-s2.0-S0168900203013688-main.pdf?_tid=2ab2887a-7a2b-4813-9966-25cc44845930&acdnat=1524482129_7273334d05ad6f2c66d093ae3c67b132)
- 943 [18] T. Bilka, N. Braun, T. Hauth, et al., Implementation of GENFIT2 as
944 an experiment independent track-fitting framework [arXiv:1902.04405](https://arxiv.org/abs/1902.04405).
945 URL <http://arxiv.org/abs/1902.04405>
- 946 [19] V. Karimäki, Effective circle fitting for particle trajectories, Nuclear
947 Instruments and Methods in Physics Research Section A: Accelerators,
948 Spectrometers, Detectors and Associated Equipment 305 (1) (1991)
949 187–191. doi:10.1016/0168-9002(91)90533-V.
950 URL [https://linkinghub.elsevier.com/retrieve/pii/
951 S016890029190533V](https://linkinghub.elsevier.com/retrieve/pii/S016890029190533V)
- 952 [20] A. Strandlie, J. Wroldsen, R. Frühwirth, B. Lillekjendlie, Particle tracks
953 fitted on the Riemann sphere, Computer Physics Communications
954 131 (1-2) (2000) 95–108. doi:10.1016/S0010-4655(00)00086-2.
955 URL [https://linkinghub.elsevier.com/retrieve/pii/
956 S0010465500000862](https://linkinghub.elsevier.com/retrieve/pii/S0010465500000862)
- 957 [21] J. Lettenbichler, Real-time Pattern Recognition in the Central Tracking
958 Detector of the Belle II Experiment, Ph.D. thesis, Technische Universität
959 Wien (2016).
960 URL <http://www.ub.tuwien.ac.at>
- 961 [22] J. Wagner, Track Finding with the Silicon Strip Detector of the Belle II
962 Experiment, Master’s thesis, Karlsruhe Institute of Technology (2017).
963 URL [https://ekp-invenio.physik.uni-karlsruhe.de/record/
964 48930/files/EKP-2017-00057.pdf](https://ekp-invenio.physik.uni-karlsruhe.de/record/48930/files/EKP-2017-00057.pdf)
- 965 [23] S. Racs, Track Quality Estimation and Defect Sensor Studies for the
966 Silicon Vertex Detector of the Belle II-Experiment, Master’s thesis,
967 Karlsruhe Institute of Technology, Karlsruhe (2018).

- 968 URL [https://ekp-invenio.physik.uni-karlsruhe.de/record/](https://ekp-invenio.physik.uni-karlsruhe.de/record/49052)
969 49052
- 970 [24] R. Frühwirth, R. Glattauer, J. Lettenbichler, W. Mitaroff, M. Nadler,
971 Track finding in silicon trackers with a small number of layers, Nuclear
972 Instruments and Methods in Physics Research Section A: Accelerators,
973 Spectrometers, Detectors and Associated Equipment 732 (2013) 95–98.
974 doi:10.1016/j.nima.2013.06.035.
975 URL [https://linkinghub.elsevier.com/retrieve/pii/](https://linkinghub.elsevier.com/retrieve/pii/S0168900213008607)
976 S0168900213008607
- 977 [25] N. Berger, A. Kozlinskiy, M. Kiehn, A. Schöning, A new three-
978 dimensional track fit with multiple scattering, Nuclear Instruments
979 and Methods in Physics Research Section A: Accelerators, Spec-
980 trometers, Detectors and Associated Equipment 844 (2017) 135–140.
981 doi:10.1016/j.nima.2016.11.012.
982 URL [https://linkinghub.elsevier.com/retrieve/pii/](https://linkinghub.elsevier.com/retrieve/pii/S016890021631138X)
983 S016890021631138X
- 984 [26] P. Billoir, Progressive track recognition with a Kalman-like fitting pro-
985 cedure, Computer Physics Communications 57 (1-3) (1989) 390–394.
986 doi:10.1016/0010-4655(89)90249-X.
987 URL [http://linkinghub.elsevier.com/retrieve/pii/](http://linkinghub.elsevier.com/retrieve/pii/001046558990249X)
988 001046558990249X[https://linkinghub.elsevier.com/retrieve/](https://linkinghub.elsevier.com/retrieve/pii/001046558990249X)
989 [pii/001046558990249X](https://linkinghub.elsevier.com/retrieve/pii/001046558990249X)
- 990 [27] E. Lund, L. Bugge, I. Gavrilenko, A. Strandlie, Track parameter propa-
991 gation through the application of a new adaptive Runge-Kutta-Nyström
992 method in the ATLAS experiment, Journal of Instrumentation 4 (04)
993 (2009) P04001–P04001. doi:10.1088/1748-0221/4/04/P04001.
994 URL [http://stacks.iop.org/1748-0221/4/i=04/a=P04001?key=](http://stacks.iop.org/1748-0221/4/i=04/a=P04001?key=crossref.4db573cdf47b35d9171ab976705899ed)
995 [crossref.4db573cdf47b35d9171ab976705899ed](http://stacks.iop.org/1748-0221/4/i=04/a=P04001?key=crossref.4db573cdf47b35d9171ab976705899ed)
- 996 [28] B. Efron, Bootstrap Methods: Another Look at the Jackknife, The An-
997 nals of Statistics 7 (1) (1979) 1–26. doi:10.1214/aos/1176344552.
998 URL <http://projecteuclid.org/euclid.aos/1176344552>